

Tetrahedral Core in a Sea of Competing Magnetic Phases in Graphene

Maxime Lucas,^{1,*} Arnaud Ralko,^{2,†} Andreas Honecker,¹ and Guy Trambly de Laissardière^{1,‡}

¹*Laboratoire de Physique Théorique et Modélisation,*

CY Cergy Paris Université, CNRS UMR8089, 95302 Cergy-Pontoise, France

²*Institut Néel, Université Grenoble Alpes, CNRS, Grenoble INP, 38000 Grenoble, France*

(Dated: December 1, 2025)

We reveal the emergence of a robust tetrahedral magnetic ground state in monolayer graphene doped to the van Hove singularity (vHS). This noncoplanar, gapped spin configuration—featuring four equally inclined moments—has been previously identified as a candidate instability. Here, not only do we confirm its stability across all finite interactions using fully self-consistent, real-space-resolved calculations, but we also go beyond earlier work by charting the full surrounding phase diagram. In doing so, we unravel a cascade of symmetry-broken magnetic states — pseudo-tetrahedral, planar, collinear, and modulated textures — which we classify using spin structure factors and vector order parameters. These results stem from unrestricted Hartree-Fock simulations on large supercells with dense k -point sampling, enabling us to resolve interaction-driven magnetic and charge inhomogeneities. Our findings connect directly with recent ARPES and doping experiments near the vHS in graphene, and establish the tetrahedral state as the central correlated instability in this regime, offering predictive insight into emergent magnetism in correlated Dirac materials.

The exploration of strongly correlated phases in two-dimensional electron systems has been revitalized by the discovery of superconductivity, Mott insulating states, and anomalous Hall effects in twisted bilayer graphene (TBG) near the “magic angle” [1–5]. In this regime, the moiré superlattice gives rise to ultra-flat electronic bands [6–9], strongly enhancing the role of electron-electron interactions and promoting exotic quantum states. A key unifying feature across these systems is the proximity of the Fermi level to van Hove singularities (vHS), where the density of states diverges and interaction effects are dramatically enhanced [9–21]. Understanding the role of vHS in driving correlated phases is thus essential not only for TBG but also for untwisted monolayer and bilayer graphene systems [22–31].

In monolayer graphene, accessing the vHS via doping remains experimentally challenging but feasible through alkali or rare-earth intercalation. Techniques involving K, Ca, Gd, and Yb atoms have allowed systematic tuning of the Fermi level and direct ARPES observation of the Dirac cone’s shift [22, 27, 28]. These studies reveal signatures of extended vHS structures induced by electronic interactions and hybridization. More recently, doping-controlled superconducting domes have been observed in bilayer graphene [29], drawing intriguing parallels with the superconducting phases in TBG.

From a theoretical perspective, numerous studies have proposed that the vHS regime in graphene—regardless of stacking—hosts a rich competition between magnetism and superconductivity. Functional renormalization group and density matrix renormalization group approaches have consistently predicted a chiral spin-density wave, also referred to as a tetrahedral magnetic order (Tetra), at quarter filling [23, 24, 30, 32, 33]. This phase competes with $d + id$ superconductivity [25], and may also give rise to spontaneous quantum anomalous Hall

effects [23, 26]. These findings are further corroborated by variational Monte Carlo simulations [31] and extended Hubbard models [26], which show robustness of the tetrahedral state against next-nearest-neighbor interactions and suggest a universal tendency toward noncoplanar magnetism near the vHS.

The relevance of noncoplanar and geometrically non-trivial spin states extends beyond graphene. Recent works in frustrated magnets report tetrahedral and cuboctahedral orders stabilized by itinerant electrons or competing exchanges. In triangular metals such as $\text{Co}_{1/3}\text{TaS}_2$, tetrahedral triple- Q order is linked to large spontaneous Hall conductivities [34], while cuboctahedral states appear in kagome antiferromagnets [35–37]. Spin-1 bilinear-biquadratic models on the honeycomb lattice also host eightfold degenerate chiral spin liquids and multipolar orders with non-zero scalar chirality, from the interplay of dipolar and quadrupolar moments [38, 39]. These developments underscore broad interest in unconventional textures across lattices and models, motivating their study in itinerant systems like doped graphene.

In this Letter, we study magnetic phases in monolayer graphene near the vHS using the Hubbard model within a non-collinear Hartree-Fock framework, resolving the interplay between filling N_e (average number of electron per orbital) and on-site Coulomb interaction U on large supercells with full reciprocal-space resolution. Building on mean-field validations at half-filling ($N_e = 1$) in graphene and twisted bilayer graphene (e.g., Refs. [20, 40–42]), we construct an ultra-low-temperature density-interaction (N_e, U) phase diagram, focusing on quarter doping ($N_e = 3/4 = 0.75$ or $5/4 = 1.25$) where correlation effects peak. Figure 1 shows that at $N_e = 0.75$ we find a *tetrahedral magnetic order* (Tetra)—a noncoplanar, three-dimensional configuration with exact tetrahedral symmetry [43]. This state is gapped and

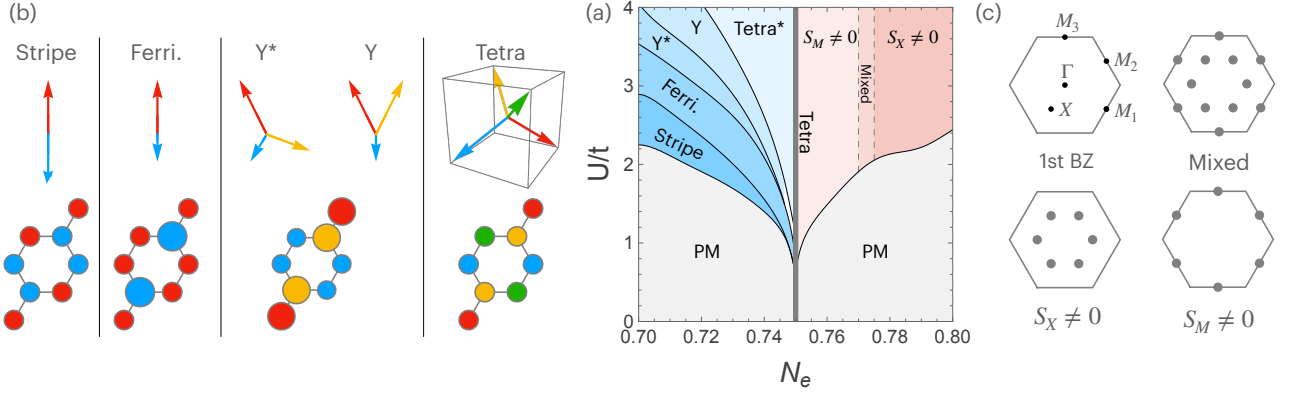


FIG. 1. Magnetic ground-state phase diagram of graphene near quarter doping. (a) Schematic mean-field (N_e, U) phase diagram based on computations at $k_B T = 10^{-7}t$, using a 6×6 supercell and 48×48 k -point sampling. (b) For doping levels below the van Hove singularity (vHS), $N_e \leq 0.75$, indicated by blue regions, all magnetic phases exhibit well-defined spin orders compatible with a 2×2 graphene supercell (see also End Matter Fig. 6). Real-space sketches illustrate these phases: “Tetra” denotes the ideal tetrahedral configuration with four spins forming a perfect tetrahedron (found only at $N_e = 0.75$); canted tetrahedral states are its distorted variants and denoted by “Tetra*”. “Y” and “Y*” refer to planar ferrimagnetic states with three distinct spin orientations, while “Ferri.” indicates a two-moment ferrimagnetic phase. “Stripe” represents a collinear magnetic phase with uniform spin magnitudes. (c) Above the vHS (red regions), more complex magnetic orders arise, strongly dependent on both doping and Coulomb interaction U . These fall into two primary regimes characterized by dominant magnetic structure factors at the high-symmetry points M_i and X in the Brillouin zone. An intermediate mixed region, where both $S_M \neq 0$ and $S_X \neq 0$, is indicated with dashed lines. Phase boundaries are defined according to the order parameters described in Fig. 2.

exhibits zero net magnetization despite long-range order. Away from quarter filling and for $U \leq 3.75t$, the magnetic landscape becomes richer: for $N_e < 0.75$ we identify phases (pseudo-tetrahedral (Tetra*), planar Y and Y*, ferrimagnetic, stripe) robust to finite-size effects, while for $N_e > 0.75$ we observe intricate, often incommensurate textures with emergent *charge density displacements*, possibly linked to local phase separation or magneto-electric coupling. These results highlight doping-driven complex spin orders in graphene and support the view that correlated phases—beyond conventional spin-density waves—play a central role near the vHS.

Model and Method.— We consider monolayer graphene described by the single-band Hubbard model on the honeycomb lattice (see, e.g., Ref. [44]),

$$H = -t \sum_{\langle i,j \rangle, \sigma} (c_{i\sigma}^\dagger c_{j\sigma} + \text{h.c.}) + U \sum_i n_{i\uparrow} n_{i\downarrow} - \mu \sum_{i\sigma} n_{i\sigma}, \quad (1)$$

where t is the nearest-neighbor hopping amplitude, U the on-site Coulomb repulsion, μ the chemical potential and $c_{i\sigma}$ ($c_{i\sigma}^\dagger$) annihilates (creates) a spin- σ electron on the p_z orbital at site i .

To investigate magnetic instabilities at finite doping, we solve this model using an unrestricted Hartree-Fock mean-field decoupling that preserves spin-rotational symmetry. Details can be found in the End Matter. This approach also enables the construction of a (N_e, U) phase diagram at low temperature, capturing both commensu-

rate magnetic phases and interaction-induced charge inhomogeneities, including nontrivial textures beyond simple spin-density waves. Further numerical details and convergence tests are provided in the End Matter as well.

Phase diagram.— Figure 1(a) presents a sketch of the (N_e, U) phase diagram computed at low temperature for $0.7 \leq N_e \leq 0.8$ and $U/t \leq 3.75$, using a 6×6 graphene supercell with 48×48 k -point sampling (see End Matter Appendix C, D for technical details). This captures the evolution of magnetic ground states near quarter doping, $N_e = 0.75$, where the Fermi level crosses the vHS. Owing to particle-hole symmetry, the same results apply to $N_e \in [1.2, 1.3]$.

At exact quarter doping ($N_e = 0.75$ or 1.25), the critical interaction U_c vanishes due to the divergent density of states at the vHS. In this limit, the system always stabilizes (with enough k -points, see End Matter Appendix C for more details) into a tetrahedral magnetic order [Fig. 1(b)], also known under different names in previous investigations [23, 24, 30–33, 45]. This noncoplanar configuration spans a 2×2 graphene supercell and consists of eight local moments pointing along the directions of a perfect tetrahedron (109.47° angles). It is the only gapped state in the phase diagram and carries zero net magnetization $\mathbf{M}_t = \mathbf{0}$.

Away from the vHS, magnetism sets in above a finite U_c that grows as N_e deviates from 0.75 , consistent with the Stoner criterion $U_c \propto 1/D(E)$, with $D(E)$ the density of states. A paramagnetic phase thus appears at low U (gray). To characterize the surrounding phases, it is

useful to distinguish between the regions below and above $N_e = 0.75$.

For $N_e < 0.75$, we identify five well-defined magnetic states, confirmed by larger supercell (24×24) calculations. Figure 6 may help to illustrate how the orders sketched in Fig. 1 tile the honeycomb lattice. As N_e decreases, these phases evolve smoothly from the tetrahedral state as: (i) a Tetra* state that is a deformation of the tetrahedral state, *i.e.*, this state still has moments pointing in four different directions, but these no longer are at exactly 109.47° angles, and the lengths also become different; (ii) a region where only three different magnetic moments appear, two of these moments are arranged symmetrically around the third one. Such a state is reminiscent of the “Y” state that is discussed in the context of the Heisenberg antiferromagnet (see Refs. [46, 47] and references therein), and therefore we use the same notation also here; (iii) going even further away from $N_e = 0.75$, the Y state distorts with three distinct magnetic moments, all of them being now nonequivalent. In analogy with the Tetra* state, we call this the “Y*” state; (iv) this Y* is then reduced to two distinct moments parallel to each other (collinear), but with different moment magnitudes. This phase is “ferromagnetic” because of the overall net magnetic moment present in the system; (v) eventually, the moment imbalance of the ferrimagnetic state vanishes letting a “stripe” order state to be stabilized, that is reminiscent of the one reported in the Heisenberg-Kitaev model on the honeycomb lattice [48, 49]. This state could be described by a reduced 2×1 supercell, compare Fig. 6(a) in the End Matter, while all other states in the region $N_e \leq 0.75$ require a 2×2 supercell (Fig. 6(b-d)). All states except the stripe and pure tetrahedral one carry a finite total magnetization. Note that small modulations of the charge density occur in the region $N_e < 0.75$, but these are commensurate with the magnetic order and thus not carrying additional information.

For $N_e > 0.75$, the phase diagram becomes more intricate. As shown in Fig. 1(c), we distinguish two regimes based on the spin structure factor for a 6×6 supercell. In the region labeled $S_M \neq 0$, magnetic orders remain quasi- 2×2 periodic, with increasingly distorted tetrahedral-like motifs. Beyond $N_e \approx 0.775$, the system enters a region labeled $S_X \neq 0$, where complex 3×3 periodic structures emerge, involving over ten nonequivalent spin orientations. The boundary between these two regions is not sharply defined, and several intermediate states display features of both (see next paragraph and Fig. 2). While the 6×6 results give clear trends, full characterization of the region $S_X \neq 0$ likely requires larger supercells and additional order parameters. Our 24×24 simulations confirm the trend toward 2×2 and 3×3 modulations in the region with $S_M \neq 0$ and $S_X \neq 0$, respectively, but also sometimes reveal charge redistribution effects – a key point discussed later.

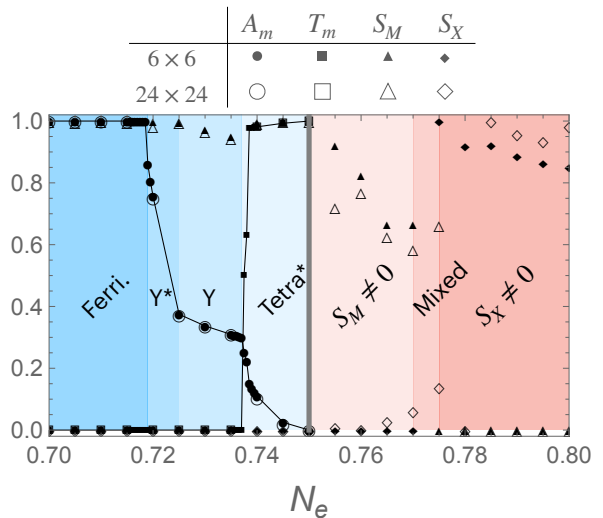


FIG. 2. Evolution of magnetic order parameters with electron density in the ground state at fixed interaction strength $U = 3t$. Upper table: Symbol correspondence with the four observables A_m , T_m , S_M , and S_X described in the text. Background colors correspond to those used characterizing the regions of the phase diagram Fig. 1. Empty (filled) symbols represent data obtained on 6×6 (24×24) supercells.

Order parameters.— To quantitatively characterize the variety of magnetic phases found in the (N_e, U) space, we employ a set of four tailored order parameters that probe both local spin configurations and global periodicities: A_m (magnetic alignment factor), scalar product between spins in a 2×2 local subcell, quantifies the average local collinearity between neighboring magnetic moments; T_m (magnetic twist vector), the cross product of four neighboring spins, is a sensitive probe to noncoplanarity among groups of spins, capturing vector chirality and geometric torsion. It is nonzero only for both the Tetra and Tetra* configurations. Note also that while local noncoplanar arrangements could in principle yield nonzero signal, such patterns were not observed in our simulations; the structure factors at high-symmetry points S_M and S_X , corresponding to 2×2 and 3×3 periodicity respectively, with the M points of the Brillouin zone being linear combinations of $\mathbf{b}_1/2$ and $\mathbf{b}_2/2$, X -point of $\mathbf{b}_1/3$ and $\mathbf{b}_2/3$ ($\mathbf{b}_1 = \frac{4\pi}{3a}(\frac{\sqrt{3}}{2}, -\frac{1}{2})$, $\mathbf{b}_2 = \frac{4\pi}{3a}(0, 1)$, where $a \approx 1.42 \text{ \AA}$ is the carbon-carbon distance). All these observables are detailed in the End Matter, and their evolution with doping, shown in Fig. 2 for $U = 3t$, is computed for both 6×6 and 24×24 supercells to verify robustness with respect to the size of the supercell.

For $N_e \leq 0.75$, the 24×24 results in Fig. 2 are very close to the 6×6 ones, thus justifying the previous discussion based on the 6×6 supercell. In particular, the different order parameters in Fig. 2 permit us to reconstruct the different phases and the transitions between

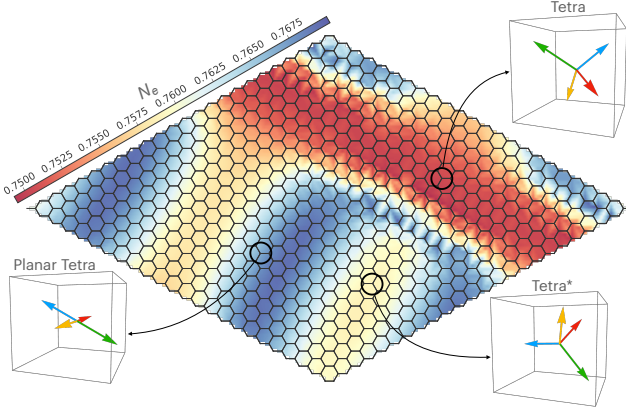


FIG. 3. Charge density in a 24×24 supercell at $U = 3t$ and average density $N_e = 0.76$. We observe non-periodic charge displacement, which creates zones of different density. The red stripe is at $N_e = 0.75$ and displays exact tetrahedral order. Blue zones show perpendicular order (4 moments perpendicular to each other, in a plane) with N_e around 0.7675. Yellow zones are at $N_e = 0.76$ and show pseudo-tetrahedral orders.

them along the line $U = 3t$ in Fig. 1, with the exception of the stripe phase that is outside the window $N_e \geq 0.7$ for $U = 3t$. For $N_e > 0.75$, the differences between the 6×6 and 24×24 supercells are larger, indicating that this region requires further attention.

Charge displacement. In the left part of the phase diagram, *i.e.*, $0.7 \leq N_e \leq 0.75$, our mean-field calculations performed in the 6×6 and the 24×24 supercells show a small charge displacement between orbitals, distributed according to the periodicity of the magnetic orders. This displacement is of the order of $\delta N_e = 5 \cdot 10^{-3}$.

In the right part of the phase diagram, we observed that size frustration (due to 6×6 supercell periodicity) may lead to perfect-looking orders which disappear for larger supercells (24×24 supercell). However, in the calculations with a larger supercell, a pseudo periodicity of the magnetic order is usually found in agreement with 2×2 and 3×3 periodicity for the zones $S_M \neq 0$ and $S_X \neq 0$, respectively.

Other cases exhibit a relatively strong charge transfer between different zones of the supercell. For instance, Fig. 3 shows that we lose the global Tetra* order to local orders: in the 24×24 supercell, we find Tetra* zones that are incompatible with a 2×2 periodicity as neighboring zones break tetrahedral behavior. The maximum difference with the start density is small (roughly ± 0.01), but essential for the magnetic orders found in each zone. The red regions in Fig. 3 have an average charge of $N_e = 0.75$ and when looking at the magnetic moments in this region, we find an exact tetrahedral order. Moving away from this zone we lose the tetrahedral angles but keep a 4-moments state, either a Tetra* order with varying an-

gles or a planar Tetra order. It remains to be checked if these spatial structures are stable for even larger supercells, but our 24×24 results underline the importance of the charge density for the magnetic order. In any case, the spontaneous formation of stripes with charge density $N_e = 0.75$ and accompanying exact tetrahedral order illustrated in Fig. 3 is remarkably reminiscent of the stripes known from the square-lattice Hubbard model for the high-temperature superconductors around filling one eighth, see, *e.g.*, Refs. [50–56]. We note that stripes have been observed also in the Hubbard model on the honeycomb lattice, albeit in the lightly doped regime, and with different methods from those employed here [57], in particular without admitting for the noncollinear solution that we find here at the mean-field level.

Conclusion.— We have mapped the magnetic phase diagram of doped monolayer graphene near the van Hove singularity using a fully unrestricted, spin-rotationally invariant Hartree-Fock approach to the Hubbard model. This framework allowed us to resolve a rich set of ground states as a function of interaction strength and carrier density, capturing both collinear and complex noncoplanar magnetic textures.

One key result is the stabilization of a fully gapped, noncoplanar tetrahedral magnetic order exactly at quarter doping ($N_e = 0.75$), where the density of states diverges. This state, characterized by zero net magnetization and 2×2 periodicity, emerges for any finite U and constitutes a rare realization of a nontrivial spin configuration in a simple one-orbital model. As doping is tuned away from the vHS, a sequence of symmetry-reduced magnetic phases arises, which we have classified using both local spin geometry and structure factor-based order parameters. These include Tetra*, Y and Y*, ferrimagnetic, and stripe states on the underdoped side ($N_e < 0.75$), and increasingly intricate incommensurate textures beyond $N_e > 0.75$, with approximate 2×2 or 3×3 periodicity.

In the latter regime, we also observe signatures of interaction-induced charge redistribution, reflected in the emergence of spatial density modulations. These suggest that the electronic correlations near the vHS may drive not only magnetic ordering but also coupling to charge degrees of freedom—possibly a precursor to intertwined or phase-separated states.

Overall, our results demonstrate that graphene doped near the vHS harbors a remarkably rich landscape of magnetic phases, several of which are both nontrivial and robust. It would be interesting to test the stability of these phases beyond the mean-field approximation. The density matrix renormalization group method suggests itself for this purpose, as it has been widely applied to the doped square-lattice Hubbard model, see, *e.g.*, Refs. [50, 54–56] and references therein. We are aware of only a few corresponding investigations on the honeycomb lattice carried out so far [30, 57, 58], and given

the inherent limitations of the accessible system sizes, we hope that our mean-field results with relatively large supercells and k -space integration will provide useful guidance for the choice of geometries to be used in future unbiased numerical investigations of graphene doped near $N_e \approx 0.75$.

Acknowledgments.— Numerical calculations have been performed at *Centre de Calculs* (CDC), CY Cergy Paris Université, and at TGCC-GENCI (Project AD010910784). We warmly thank Yann Costes and Baptiste Mary, CDC, for computing assistance. We acknowledge financial support from the ANR FlatMoi project (ANR-21-CE30-0029).

* maxime.lucas-guerreau@cyu.fr

† arnaud.ralko@neel.cnrs.fr

‡ guy.trambly@cyu.fr

- [1] Y. Cao, V. Fatemi, A. Demir, S. Fang, S. L. Tomarken, J. Y. Luo, J. D. Sanchez-Yamagishi, K. Watanabe, T. Taniguchi, E. Kaxiras, R. C. Ashoori, and P. Jarillo-Herrero, Correlated insulator behaviour at half-filling in magic-angle graphene superlattices, *Nature* **556**, 80 (2018).
- [2] Y. Cao, V. Fatemi, S. Fang, K. Watanabe, T. Taniguchi, E. Kaxiras, and P. Jarillo-Herrero, Unconventional superconductivity in magic-angle graphene superlattices, *Nature* **556**, 43 (2018).
- [3] Y. Sherkunov and J. J. Betouras, Electronic phases in twisted bilayer graphene at magic angles as a result of van Hove singularities and interactions, *Phys. Rev. B* **98**, 205151 (2018).
- [4] D. Guerci, P. Simon, and C. Mora, Higher-order van Hove singularity in magic-angle twisted trilayer graphene, *Phys. Rev. Res.* **4**, L012013 (2022).
- [5] Y. H. Kwan, J. Yu, J. Herzog-Arbeitman, D. K. Efetov, N. Regnault, and B. A. Bernevig, Moiré fractional Chern insulators. III. Hartree-Fock phase diagram, magic angle regime for Chern insulator states, role of moiré potential, and Goldstone gaps in rhombohedral graphene superlattices, *Phys. Rev. B* **112**, 075109 (2025).
- [6] G. Trambly de Laissardiére, D. Mayou, and L. Magaud, Localization of Dirac electrons in rotated graphene bilayers, *Nano Letters* **10**, 804 (2010).
- [7] E. Suárez Morell, J. D. Correa, P. Vargas, M. Pacheco, and Z. Barticevic, Flat bands in slightly twisted bilayer graphene: Tight-binding calculations, *Phys. Rev. B* **82**, 121407(R) (2010).
- [8] R. Bistritzer and A. H. MacDonald, Transport between twisted graphene layers, *Phys. Rev. B* **81**, 245412 (2010).
- [9] G. Trambly de Laissardiére, S. Venkateswarlu, A. Missaoui, G. Jemai, K. Chika, J. Vahedi, O. Faizy Nammarvar, J.-P. Julien, A. Honecker, L. Magaud, J. Jemaa Khabthani, and D. Mayou, Electronic structure and transport in materials with flat bands: 2D materials and quasicrystals, *Physica E* **175**, 116362 (2026).
- [10] L. A. Gonzalez-Arraga, J. L. Lado, F. Guinea, and P. San-Jose, Electrically controllable magnetism in twisted bilayer graphene, *Phys. Rev. Lett.* **119**, 107201 (2017).
- [11] Y.-W. Liu, J.-B. Qiao, C. Yan, Y. Zhang, S.-Y. Li, and L. He, Magnetism near half-filling of a van Hove singularity in twisted graphene bilayer, *Phys. Rev. B* **99**, 201408 (2019).
- [12] Y. Choi, J. Kemmer, Y. Peng, A. Thomson, H. Arora, R. Polski, Y. Zhang, H. Ren, J. Alicea, G. Refael, F. von Oppen, K. Watanabe, T. Taniguchi, and S. Nadj-Perge, Electronic correlations in twisted bilayer graphene near the magic angle, *Nat. Phys.* **15**, 1174 (2019).
- [13] Y. Xie, B. Lian, B. Jäck, X. Liu, C. L. Chiu, K. Watanabe, T. Taniguchi, B. A. Bernevig, and A. Yazdani, Spectroscopic signatures of many-body correlations in magic-angle twisted bilayer graphene, *Nature* **572**, 101 (2019).
- [14] Y. Jiang, J. Mao, X. Lai, K. Watanabe, T. Taniguchi, K. Haule, and E. Y. Andrei, Charge order and broken rotational symmetry in magic-angle twisted bilayer graphene, *Nature* **573**, 91 (2019).
- [15] A. L. Sharpe, E. J. Fox, A. W. Barnard, J. Finney, K. Watanabe, T. Taniguchi, M. A. Kastner, and D. Goldhaber-Gordon, Emergent ferromagnetism near three-quarters filling in twisted bilayer graphene, *Science* **365**, 605 (2019).
- [16] L. Klebl and C. Honerkamp, Inherited and flatband-induced ordering in twisted graphene bilayers, *Phys. Rev. B* **100**, 155145 (2019).
- [17] M. Xie and A. H. MacDonald, Nature of the correlated insulator states in twisted bilayer graphene, *Phys. Rev. Lett.* **124**, 097601 (2020).
- [18] F. Mesple, A. Missaoui, T. Cea, L. Huder, F. Guinea, G. Trambly de Laissardiére, C. Chapelier, and V. T. Renard, Heterostrain determines flat bands in magic-angle twisted graphene layers, *Phys. Rev. Lett.* **127**, 126405 (2021).
- [19] Y. Choi, H. Kim, Y. Peng, A. Thomson, C. Lewandowski, R. Polski, Y. Zhang, H. S. Arora, K. Watanabe, T. Taniguchi, J. Alicea, and S. Nadj-Perge, Correlation-driven topological phases in magic-angle twisted bilayer graphene, *Nature* **589**, 536 (2021).
- [20] J. Vahedi, R. Peters, A. Missaoui, A. Honecker, and G. Trambly de Laissardiére, Magnetism of magic-angle twisted bilayer graphene, *SciPost Phys.* **11**, 83 (2021).
- [21] G. Wagner, Y. H. Kwan, N. Bultinck, S. H. Simon, and S. A. Parameswaran, Global phase diagram of the normal state of twisted bilayer graphene, *Phys. Rev. Lett.* **128**, 156401 (2022).
- [22] J. L. McChesney, A. Bostwick, T. Ohta, T. Seyller, K. Horn, J. González, and E. Rotenberg, Extended van Hove singularity and superconducting instability in doped graphene, *Phys. Rev. Lett.* **104**, 136803 (2010).
- [23] T. Li, Spontaneous quantum Hall effect in quarter-doped Hubbard model on honeycomb lattice and its possible realization in doped graphene system, *EPL* **97**, 37001 (2012).
- [24] W.-S. Wang, Y.-Y. Xiang, Q.-H. Wang, F. Wang, F. Yang, and D.-H. Lee, Functional renormalization group and variational Monte Carlo studies of the electronic instabilities in graphene near $\frac{1}{4}$ doping, *Phys. Rev. B* **85**, 035414 (2012).
- [25] R. Nandkishore, L. S. Levitov, and A. V. Chubukov, Chiral superconductivity from repulsive interactions in doped graphene, *Nature Phys.* **8**, 158 (2012).
- [26] K. Jiang, Y. Zhang, S. Zhou, and Z. Wang, Chiral spin density wave order on the frustrated honeycomb and bilayer triangle lattice Hubbard model at half-filling, *Phys.*

- Rev. Lett.* **114**, 216402 (2015).
- [27] S. Link, S. Forti, A. Stöhr, K. Küster, M. Rösner, D. Hirschmeier, C. Chen, J. Avila, M. C. Asensio, A. A. Zakharov, T. O. Wehling, A. I. Lichtenstein, M. I. Katsnelson, and U. Starke, Introducing strong correlation effects into graphene by gadolinium intercalation, *Phys. Rev. B* **100**, 121407 (2019).
 - [28] P. Rosenzweig, H. Karakachian, S. Link, K. Küster, and U. Starke, Tuning the doping level of graphene in the vicinity of the van Hove singularity via ytterbium intercalation, *Phys. Rev. B* **100**, 035445 (2019).
 - [29] W. Wan, R. Harsh, P. Dreher, F. de Juan, and M. M. Ugeda, Superconducting dome by tuning through a van Hove singularity in a two-dimensional metal, *npj 2D Mater. Appl.* **7**, 41 (2023).
 - [30] S. Jiang, A. Mesaros, and Y. Ran, Chiral spin-density wave, spin-charge-Chern liquid, and $d + id$ superconductivity in 1/4-doped correlated electronic systems on the honeycomb lattice, *Phys. Rev. X* **4**, 031040 (2014).
 - [31] T. Ying and S. Wessel, Pairing and chiral spin density wave instabilities on the honeycomb lattice: A comparative quantum Monte Carlo study, *Phys. Rev. B* **97**, 075127 (2018).
 - [32] P. H. Wilhelm, T. C. Lang, M. S. Scheurer, and A. M. Läuchli, Non-coplanar magnetism, topological density wave order and emergent symmetry at half-integer filling of moiré Chern bands, *SciPost Phys.* **14**, 040 (2023).
 - [33] R. Scholle and L. Classen, Mean-field analysis of a Hubbard interaction on bernal bilayer graphene (2024), [arXiv:2412.15945](https://arxiv.org/abs/2412.15945).
 - [34] P. Park, W. Cho, C. Kim, Y. An, Y.-G. Kang, M. Avdeev, R. Sibille, K. Iida, R. Kajimoto, K. H. Lee, W. Ju, E.-J. Cho, H.-J. Noh, M. J. Han, S.-S. Zhang, C. D. Batista, and J.-G. Park, Tetrahedral triple-Q magnetic ordering and large spontaneous Hall conductivity in the metallic triangular antiferromagnet $\text{Co}_{1/3}\text{TaS}_2$, *Nat. Commun.* **14**, 8346 (2023).
 - [35] L. Messio, B. Bernu, and C. Lhuillier, Kagome antiferromagnet: A chiral topological spin liquid?, *Phys. Rev. Lett.* **108**, 207204 (2012).
 - [36] L. Messio, C. Lhuillier, and G. Misguich, Time reversal symmetry breaking chiral spin liquids: Projective symmetry group approach of bosonic mean-field theories, *Phys. Rev. B* **87**, 125127 (2013).
 - [37] T. Lugan, L. D. C. Jaubert, M. Udagawa, and A. Ralko, Schwinger boson theory of the $J_1, J_2 = J_3$ kagome antiferromagnet, *Phys. Rev. B* **106**, L140404 (2022).
 - [38] R. Pohle, N. Shannon, and Y. Motome, Spin nematics meet spin liquids: Exotic quantum phases in the spin-1 bilinear-biquadratic model with Kitaev interactions, *Phys. Rev. B* **107**, L140403 (2023).
 - [39] R. Pohle, N. Shannon, and Y. Motome, Eight-color chiral spin liquid in the $S = 1$ bilinear-biquadratic model with Kitaev interactions, *Phys. Rev. Res.* **6**, 033077 (2024).
 - [40] S. Sorella and E. Tosatti, Semi-metal-insulator transition of the Hubbard model in the honeycomb lattice, *EPL* **19**, 699 (1992).
 - [41] H. Feldner, Z. Y. Meng, A. Honecker, D. Cabra, S. Wessel, and F. F. Assaad, Magnetism of finite graphene samples: Mean-field theory compared with exact diagonalization and quantum Monte Carlo simulations, *Phys. Rev. B* **81**, 115416 (2010).
 - [42] M. Raczkowski, R. Peters, T. T. Phung, N. Takemori, F. F. Assaad, A. Honecker, and J. Vahedi, Hubbard model on the honeycomb lattice: From static and dynamical mean-field theories to lattice quantum Monte Carlo simulations, *Phys. Rev. B* **101**, 125103 (2020).
 - [43] This holds for all $U/t \leq 3.75$ studied; behavior at larger U is beyond this work.
 - [44] O. V. Yazyev, Emergence of magnetism in graphene materials and nanostructures, *Rep. Prog. Phys.* **73**, 056501 (2010).
 - [45] R. Nandkishore, G.-W. Chern, and A. V. Chubukov, Itinerant half-metal spin-density-wave state on the hexagonal lattice, *Phys. Rev. Lett.* **108**, 227204 (2012).
 - [46] M. V. Gvozdkova, P.-E. Melchy, and M. E. Zhitomirsky, Magnetic phase diagrams of classical triangular and kagome antiferromagnets, *J. Condens. Matter Phys.* **23**, 164209 (2011).
 - [47] C. A. Gallegos, S. Jiang, S. R. White, and A. L. Chernyshev, Phase diagram of the easy-axis triangular-lattice $J_1 - J_2$ model, *Phys. Rev. Lett.* **134**, 196702 (2025).
 - [48] J. Chaloupka, G. Jackeli, and G. Khaliullin, Zigzag magnetic order in the iridium oxide Na_2IrO_3 , *Phys. Rev. Lett.* **110**, 097204 (2013).
 - [49] J. Oitmaa, Phase diagram of the Heisenberg-Kitaev model at $T = 0$, *Phys. Rev. B* **92**, 020405 (2015).
 - [50] S. R. White and D. J. Scalapino, Density matrix renormalization group study of the striped phase in the 2D t - J model, *Phys. Rev. Lett.* **80**, 1272 (1998).
 - [51] R. F. Service, Could charge stripes be a key to superconductivity?, *Science* **283**, 1106 (1999).
 - [52] E. Berg, E. Fradkin, S. A. Kivelson, and J. M. Tranquada, Striped superconductors: how spin, charge and superconducting orders intertwine in the cuprates, *New J. Phys.* **11**, 115004 (2009).
 - [53] J. M. Tranquada, Spins, stripes, and superconductivity in hole-doped cuprates, *AIP Conf. Proc.* **1550**, 114 (2013).
 - [54] H.-C. Jiang and T. P. Devereaux, Superconductivity in the doped Hubbard model and its interplay with next-nearest hopping t' , *Science* **365**, 1424 (2019).
 - [55] A. Wietek, Fragmented Cooper pair condensation in striped superconductors, *Phys. Rev. Lett.* **129**, 177001 (2022).
 - [56] H. Xu, C.-M. Chung, M. Qin, U. Schollwöck, S. R. White, and S. Zhang, Coexistence of superconductivity with partially filled stripes in the Hubbard model, *Science* **384**, eadh7691 (2024).
 - [57] X. Yang, H. Zheng, and M. Qin, Stripe order in the doped Hubbard model on the honeycomb lattice, *Phys. Rev. B* **103**, 155110 (2021).
 - [58] C. Peng, D. N. Sheng, and H.-C. Jiang, Superconductivity in the lightly doped Hubbard model on the cylindrical honeycomb lattice, *Phys. Rev. B* **111**, 085108 (2025).
 - [59] T. T. Phung, *Numerical studies of magnetism and transport properties in graphene nanodevices*, *Phd thesis*, Université de Cergy-Pontoise, France (2019).
 - [60] R. Scholle, P. M. Bonetti, D. Vilardi, and W. Metzner, Comprehensive mean-field analysis of magnetic and charge orders in the two-dimensional Hubbard model, *Phys. Rev. B* **108**, 035139 (2023).

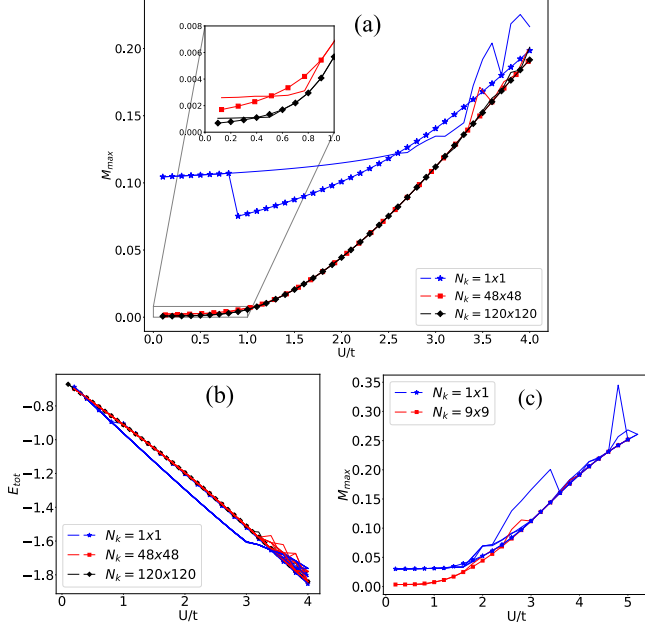


FIG. 4. Maximum local magnetic moment as a function of the Coulomb interaction U for different values of N_k , at $N_e = 0.75$. Panels (a) and (b) are for a 6×6 supercell, while (c) results from a 24×24 supercell. Lines without markers indicate results using a random initial state, while marked lines are for simulations that started from exact tetrahedral state. The inset in panel (a) shows the shift between $N_k = 48 \times 48$ and $N_k = 120 \times 120$ at low U .

END MATTER

Appendix A: Self-consistent mean-field calculation– The interaction term is decoupled in a rotationally invariant Hartree-Fock mean-field approximation as [59, 60],

$$H_U^{\text{MFT}} = U \sum_i \left[\langle n_{i\downarrow} n_{i\uparrow} + \langle n_{i\uparrow} n_{i\downarrow} - \langle n_{i\uparrow} \rangle \langle n_{i\downarrow} \rangle - \langle S_i^- \rangle S_i^+ - \langle S_i^+ \rangle S_i^- + \langle S_i^+ \rangle \langle S_i^- \rangle \right], \quad (2)$$

where $S_i^+ = c_{i\uparrow}^\dagger c_{i\downarrow}$ and $S_i^- = c_{i\downarrow}^\dagger c_{i\uparrow}$. Most previous investigations concentrated on $N_e = 1$ where one may neglect the S^\pm expectation values and simplify to a Hartree approximation (see, e.g., Refs. [9, 20, 41, 42, 44]). Inclusion of these mean fields allows us to capture arbitrary spin textures that we find to be essential for a description of the behavior close to the vHS. We note that the case $U = 3t$ has recently been investigated at finite temperature [33].

The local magnetization $\mathbf{M}_i = (M_x^i, M_y^i, M_z^i)$ and local density N_e^i are defined as,

$$\begin{aligned} M_x^i &= \frac{\langle S_i^+ \rangle + \langle S_i^- \rangle}{2}, & M_y^i &= \frac{\langle S_i^+ \rangle - \langle S_i^- \rangle}{2i}, \\ M_z^i &= \frac{\langle n_{i\uparrow} \rangle - \langle n_{i\downarrow} \rangle}{2}, & N_e^i &= \langle n_{i\uparrow} \rangle + \langle n_{i\downarrow} \rangle. \end{aligned} \quad (3)$$

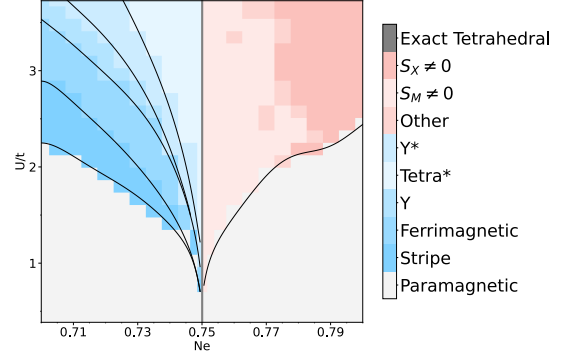


FIG. 5. Raw data for the magnetic ground-state phase diagram, with the corresponding transition lines used for the schematic Fig. 1(a). Ground states were selected among 4 sets of results, each with different initial states (Random, Tetra, Y, and Ferri), using lowest total energy per site as the selection criterion.

We solve these self-consistency conditions by iteration. Using the initial densities at every site i of the $L \times L$ supercell ($\langle n_{i\downarrow} \rangle, \langle n_{i\uparrow} \rangle, \langle S_i^+ \rangle, \langle S_i^- \rangle$), the $2\mathcal{N} \times 2\mathcal{N}$ matrix Hamiltonian (Eq. (1) with (2)) is written in the basis of the \mathcal{N} p_z orbitals, $\mathcal{N} = 2L^2$ (the factor 2 is due to the spin), and it is diagonalized in reciprocal space to obtain eigenvectors $\Psi_n(\mathbf{k})$ and eigenvalues $E_n(\mathbf{k})$. We then compute new densities to be used as input for the next iteration by defining the spinor $\Phi = [c_{i,\uparrow}, c_{i,\downarrow}]^T$ such that our mean-field parameters are defined by the matrix \mathcal{M} as $\langle \Phi^\dagger \mathcal{M} \Phi \rangle$ whose elements are given by,

$$\mathcal{M}_{\alpha\beta} = \sum_{\mathbf{k}, n} \psi_{n,i,\alpha}^*(\mathbf{k}) \psi_{n,i,\beta}(\mathbf{k}) n_{\text{FD}}(E_n(\mathbf{k}), \mu), \quad (4)$$

where $\psi_{n,i} = \langle i \uparrow | \Psi_n(\mathbf{k}) \rangle$ and $\psi_{n,i+\mathcal{N}} = \langle i \downarrow | \Psi_n(\mathbf{k}) \rangle$, $i = 1, \dots, \mathcal{N}$, are the components of $\Psi_n(\mathbf{k})$ in the p_z orbitals basis with spin \uparrow and \downarrow . \mathbf{k} are the momenta on the grid N_k in the unit cell of the reciprocal lattice corresponding to the $L \times L$ supercell ($L = 6$ and $L = 24$, i.e., $\mathcal{N} = 72$ and $\mathcal{N} = 1152$ sites in a supercell, respectively). n_{FD} is the Fermi-Dirac function, $n_{\text{FD}} = 1/(1 + e^{(E_n(\mathbf{k}) - \mu)/k_B T})$ at a non-zero temperature T . The new densities are compared with the previous densities, and the process is repeated until their difference is less than a certain threshold (usually going below 10^{-7} does not change the results). Results presented in this Letter have been obtained for a finite but ultra-low-temperature $k_B T = 10^{-7}t$. For each iteration the chemical potential μ is calculated by a bisection search around the Fermi energy. Equation (3) yields the final magnetic state of the system.

Appendix B: Spin structure factor– To analyze the magnetic order in phases with no obvious periodicity or with pseudo-periodicity, it is useful to calculate the spin struc-

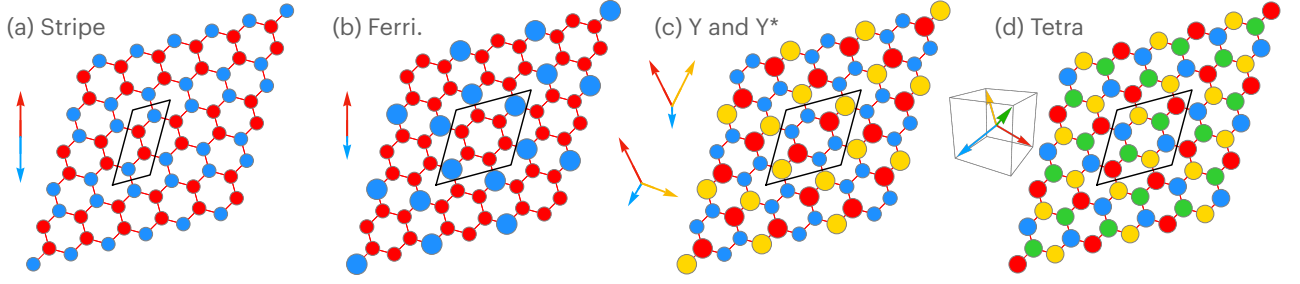


FIG. 6. Real-space magnetic configurations for $N_e \leq 0.75$. Two-dimensional snapshots of the main magnetic patterns obtained in the 6×6 supercell. Each colored disk represents a lattice site, where the color encodes the local spin orientation (angle), and the disk size is proportional to the magnitude of the local magnetic moment. Panels (a)–(d) correspond respectively to the stripe ($U = 2.58t$, $N_e = 0.71$), ferrimagnetic ($U = 2.83t$, $N_e = 0.72$), Y/Y* ($U = 3t$, $N_e = 0.73$), and tetrahedral/tetrahedral* ($U = 3t$, $N_e = 0.75$) states. Each configuration is well stabilized at the chosen U and N_e values, but represent their respective phases. The black outline marks the smallest supercell compatible with each magnetic order. These maps visualize the spin textures in real space and correspond to the spin configurations shown below each panel.

ture factor,

$$S(\mathbf{q}) = \sum_{\mathbf{R}} e^{i\mathbf{q} \cdot \mathbf{R}} \sum_{i,j}^{\mathcal{N}} \mathbf{M}_i \cdot \mathbf{M}_j e^{i\mathbf{q} \cdot (\mathbf{r}_j - \mathbf{r}_i)}, \quad (5)$$

where \mathbf{r}_i are the \mathcal{N} site positions in the $L \times L$ supercell. The sum on the vectors \mathbf{R} of the $L \times L$ supercell switches off $S(\mathbf{q})$ for any \mathbf{q} other than $\mathbf{q} = \frac{n_1}{L}\mathbf{b}_1 + \frac{n_2}{L}\mathbf{b}_2$, where $\mathbf{b}_1 = \frac{4\pi}{3a}(\frac{\sqrt{3}}{2}, -\frac{1}{2})$, $\mathbf{b}_2 = \frac{4\pi}{3a}(0, 1)$ are the reciprocal vectors of 1×1 graphene and $n_1, n_2 \in \mathbb{Z}$.

Appendix C: Importance of the k integration– In Figs. 4(a) and 4(c), the maximum local moment for $N_e = 0.75$ versus U is compared for different k -grids (N_k) used for the integration in the reciprocal unit cell for 6×6 and 24×24 supercells, respectively. The corresponding energies for 6×6 are shown in Fig. 4(b). The first result is that for large N_k , *i.e.*, for the most accurate calculation, the Tetra magnetic solution is always the most stable (lowest-energy state). Moreover, we see that for many calculations in the 6×6 and 24×24 supercells, $N_k = 1 \times 1$ is not sufficient to obtain the real ground state (Tetra), as the maximum moment values are large compared to other results.

Appendix D: Calculated phase diagram– Fig. 5 shows our calculated raw data for the magnetic ground-state phase diagram, and Fig. 6 shows the magnetic configurations in the 6×6 supercell found at $N_e \leq 0.75$. To determine the different domains, we used several order parameters (see also Fig. 2). The scalar product was mainly utilized for the transition between the Ferrimagnetic and Y orders using the sharp change in value (we can see the heavy drop around $N_e = 0.7175$), although it was also useful to confirm the transition going from Y to pseudo-

tetrahedral (Tetra*). We define this magnetic alignment thanks to the average of the spin-spin correlations within a supercell as:

$$A_m = \sum_{i,j}^{N_{\text{zone}}} \frac{\mathbf{M}_i \cdot \mathbf{M}_j}{\|\mathbf{M}_i\| \|\mathbf{M}_j\|}, \quad (6)$$

where N_{zone} corresponds to sites inside a 2×2 subcell in the middle of our 6×6 lattice. Similarly, the vector product was used for detecting the appearance of the Tetra* order. Indeed, as defined below, this parameter yields zero for the previous order (Y and Y*) while it is non-zero for Tetra*. We call the corresponding magnetic twist order parameter,

$$T_m = \frac{\|(\mathbf{M}_0 \times \mathbf{M}_1) \times (\mathbf{M}_2 \times \mathbf{M}_3)\|}{\|\mathbf{M}_0\| \|\mathbf{M}_1\| \|\mathbf{M}_2\| \|\mathbf{M}_3\|}. \quad (7)$$

The above order parameters made it possible to accurately determine the boundaries of the domains in the left-hand part of the phase diagram ($N_e \leq 0.75$), with exactly the same magnetic order found for the 6×6 (Fig. 6) and 24×24 supercell calculations (see, *e.g.*, Fig. 2).

As explained in the main text, the results obtained on the right-hand side ($N_e > 0.75$) are not identical for calculations in the 6×6 and 24×24 supercells. However, the orders found in the smaller supercell (6×6) are often also found locally also in the larger one (24×24). A criterion common to calculations in both cells is the non-zero value of the spin structure factor (Eq. (5)) for specific \mathbf{q} : $S_M = S(\mathbf{q} = \mathbf{M})$ and $S_X = S(\mathbf{q} = \mathbf{X})$ corresponding to 2×2 and 3×3 periodicity (or approximate periodicity), respectively (see Fig. 1(c)).